**Proceedings of ASME Turbo Expo 2022
Turbomachinery Technical Conference and Exposition
GT2022
June 13-17, 2022, Rotterdam, The Netherlands**

GT2022-81577

REAL TIME MGT PERFORMANCE ASSESSMENT TOOL: COMPREHENSIVE TRANSIENT BEHAVIOUR PREDICTION WITH COMPUTATIONALLY EFFECTIVE TECHNIQUES

Aggelos Gaitanis*
Université Catholique de Louvain,
University of Mons (UMONS)
Louvain la Neuve, Belgium

Francesco Contino
Université Catholique de Louvain
Thermodynamics and
fluid mechanics - TFL
Louvain la Neuve, Belgium

Ward De Paepe
University of Mons (UMONS)
Thermal Engineering and
Combustion Unit
Mons, Belgium

ABSTRACT

Conventional centralized power generation is increasingly transforming into a more distributed structure due to the transition towards more renewable energy sources. The periodic power production that is created by the renewable production unit generate the need for small-scale heat and power units. One of the promising technologies which can assist a flexible and renewable power grid is micro Gas Turbines (mGTs). Such engines are generally considered to have an electrical power output less than $500\,\mathrm{kW_e}$ *and are competent candidates for small-scale Combined Heat and Power (CHP). mGTs, as compensators for the demand fluctuations, are required to work on transient and part-load conditions. Therefore, the connection of such unit to a non-dispatchable energy system creates new research challenges.*

A complete characterization of their dynamic behaviour through a real-time simulation tool is necessary to establish effective and suitable control systems. This model should predict all the crucial parameters of the engine, such as the surge margin and combustion stability, which assist in the effective performance diagnosis. Moreover, the energy transition requires the conversion of conventional mGTs to more sophisticated high-efficient cycles with the addition of extra components (saturation unit, aftercooler, etc). Consequently, a modular and computationally fast real-time tool offers an asset in the development of future advanced cycles based on the mGT concept.

This paper presents the complete development of a numerical in-house tool implemented in the Python open-source programming language for the behaviour prediction of the mGT. The fundamental target of our work is to achieve high fidelity of the simulated dynamic responses by adopting modern coding techniques that decrease the computational time. The model is validated with experimental results from the VUB Turbec T100 test rig and with additional data published in the literature. The component modeling methods are also compared to other techniques to confirm the practicality of the current code. Key benefits of this tool are the low complexity highly efficient component modules. This code reproduces the experimental results well during transient operation as the important cycle parameters present a deviation from the measurements within the range of 1.5%.

NOMENCLATURE

Acronyms

CC	Combustion Chamber
CFD	Computational Fluid Dynamics
CHP	Combined Heat and Power
GT	Gas Turbine
RICE	Reciprocating Internal Combustion Engine
mGT	Micro Gas Turbine
mHAT	Micro Humid Air Turbine

*Address all correspondence to this author. Tel: +32 10 47 22 00 Email: angelos.gaitanis@uclouvian.be

ODE	Ordinary Differential Equation	
RMSE	Root Mean Squared Error	
TIT	Turbine Inlet Temperature	°C
TOT	Turbine Outlet Temperature	°C
VUB	Vrije Universiteit Brussel	

Roman symbols

C_p	heat capacity	kJ/(kgK)
h	specific enthalpy	J/kg
I	moment inertia	kgm^3
k	heat capacity ratio	
m	mass	kg
$\dot{m}$	mass flow rate	kg/s
N	rotational speed	rpm
n	number of cells	
P	power	kW
p	pressure	Pa
$\dot{Q}$	heat flux	kW
T	temperature	°C
t	time	s
UA	heat transfer coefficient times surface	W/K

Greek symbols

η	efficiency	
π	pressure ratio	
ρ	density	kg/m^3

INTRODUCTION

The global energy demand for industrial heat and power is steadily increasing through the years. Single power plant systems have started to be taken over by decentralised grids or smart systems [1]. Such a pathway is considered by the research community as essential to accomplish comprehensive infiltration of renewable energy sources [2]. During the renewable energy transition period, thermal power units will ensure the flexibility and security of energy supply. Thus, the need for more efficient and profitable power production by fossil fuels remains quite significant to achieve the pollutant emission targets. In such context, small-scale power production applications in a Combined Heat and Power (CHP) frameworks, which can reach an overall efficiency above 90%, could play a crucial role in the upcoming years. A prominent competitor in the CHP market, that show great potential, is micro Gas Turbine (mGT) [3].

Developed in the 1980s originally by the automotive industry, mGTs are utilized for small-scale CHP applications for over 20 years [4]. Such machines are generally defined as recuperated Gas Turbines (GT) with an electrical power output between 15 and 500 kW_e [5] that operate at high rotational speed, between 50.000 and 120.000 rpm [6]. Their multi-fuel potential associated with low emissions (especially NO_x) and maintenance costs allow them to compete against the Reciprocating Internal Combustion Engines (RICE) which dominate the CHP market [7]. Despite their lower electrical efficiency compared to the RICEs, mGTs have regained scientific and industrial interest due to the increasing tendency in more restrictive emission policies and the rise of alternative fuels. Moreover, the interest in improved efficiency concepts like the micro Humid Air Turbine (mHAT) [8] or the Aurelia A400 [9], has increased the past years.

Within this frame of reference, mGT performance should change flexibly in response to the fluctuating demand of a modern power grid. Such power production engine has to change operating points quickly and work at part load efficiently. Furthermore, during periods with fluctuating demand, the healthy operation of the compressor could be compromised due to deterioration [10]. Therefore, it is important to develop or work with a reliable dynamic model that can rather precisely and fast predict the evolution of all the important performance parameters of the engine in transient conditions.

At first, CFD approaches can assist in the enhancement of operating flexibility for each component. For instance, the development of novel combustor designs and modes can be achieved with the use of CFD analysis [11]. However, the incorporation of novel components in mGT plants, for example fuel cells, heat exchangers or saturators, significantly modify the dynamic characteristics of the system and affects the operational requirements of the turbomachinery components. Thus, modular and flexible software that simulate not only steady-state but also dynamic operation are undeniably necessary for the correct development of such novel concepts.

A number of papers, that examine the dynamic phenomena in mGT cycles, have been published. Di Gaeta et al. presented a dynamic model of the Turbec T100 without paying so much attention to the formulation of the partial differential equations expressing unsteady phenomena. He instead focused on the sensitivity of various parameters with different fuel mixtures [12]. Traverso developed and validated a modular software of the same mGT which is called TRANSEO [13]. For the dynamic computation of the energy equation of recuperator, the heat exchanger is discretized into n cells. Also a simplified "lumped volume" approach for the continuity and momentum equations is developed [14]. Furthermore, Henke et al. pursued an approach quite close to the one of Traverso regarding the flow formulation. He also focused on the extensive description of a recuperator module by analytically calculating the heat transfer coefficients [15].

The mGT models, that are cited above, definitively present many advantages concerning the correct performance prediction. Although, the relation between accuracy, calculation time, and overall complexity still remains to be investigated, particularly in the field of small-scale power production. Therefore, we aim to assemble the most effective group of modeling techniques in a control application which determines the real-time performance of such engine.

In this paper, we thoroughly describe the development of an accurate and efficient real-time mGT simulation tool. At first, we discuss the modeling strategies that were adopted and focus on the development of the turbomachinery components by accurately including the performance maps with fitting analytical relations. Moreover, each module is presented by the mathematical equations that govern it. We emphasize on the connection between the modules to remove the complexity of the code. Measurements on the T100 test rig allow us to calibrate and validate the model in steady-state conditions. Then the model's fidelity in transient mode is tested by comparing important performance values with experimental data in positive and negative step changes of the demanded power. The simulation followed the experimental data well and proved to work accurately for the modeling of mGTs.

METHODOLOGY

For the purposes of the current study, a hybrid or grey box modeling approach is followed. Such technique combines the advantages of physical and data driven models to decrease the complexity and increase the accuracy. It is rather typical to introduce this hybridization when the performance maps are incorporated. Blotenberg [16] and Bettocchi et al. [17] utilized such models for the components of a GT at the end of 1990s. They evaluated the GT shaft speed and power during a transient. In the next years, grey models have become a common practice for the dynamic modeling of large and small-scale GTs. Mathematical correlations are used for enhancing the accurate simulation of the heat transfer in the recuperator. These equations are derived from experimental data and contribute to the above mentioned hybridization as well. Therefore, in this chapter, we first introduce our technique for the inclusion of performance maps in the simulation tool and then we describe each component/module and their governing equations.

Performance maps

The performance maps for the compressor and turbine components are incorporated by fitting the accessible map data with a specific mathematical equation. More specifically, a single fitting equation for each compressor map iso-speed line is used. This formula is adjusted by its coefficients, which are functions of the reduced shaft speed. The map data of the of the turbomachinery part is provided by the manufacturer. The accuracy of our fitting techniques depends solely on the correct digitization of the maps and the structure of the mathematical formula. Therefore, to test our equations, we analysed 3 fitting cases for the calculation of mass flow rate and isentropic efficiency for the compressor and turbine. The equation that minimizes the Root Mean Squared Error (RMSE) from the data points is integrated in the simulation tool.

For the calculation of reduced mass flow rate $\dot{m}_{c,\mathrm{red}}$ in relation to pressure ratio π_c and reduced speed $N/\sqrt{T}$, three fitting curves are proposed and tested:

$$Ellipse: \left|\frac{\dot{m}^*_{c,\mathrm{red}}}{\alpha_c}\right|^2 + \left|\frac{\pi^*_c}{b_c}\right|^2 = 1 \tag{1}$$

$$Superellipse: \left|\frac{\dot{m}^*_{c,\mathrm{red}}}{\alpha_c}\right|^{n_0} + \left|\frac{\pi^*_c}{b_c}\right|^{n_0} = 1 \tag{2}$$

$$Supershape: \left|\frac{\dot{m}_{c,\mathrm{red}} - x_{0,c}}{\alpha_c}\right|^{n_1} + \left|\frac{\pi_c}{b_c}\right|^{n_2} = 1 \tag{3}$$

Equations 1 and 2 can rotate in the pressure ratio and reduced mass flow plane. As a result, an extra degree of freedom is added (θ_{π_c}) and included with two equations: $\dot{m}^*_{c,\mathrm{red}} = \dot{m}_{c,\mathrm{red}} cos(\theta_c) - \pi_c sin(\theta_c)$ and $\pi^*_c = \dot{m}_{c,\mathrm{red}} sin(\theta_c) - \pi_c cos(\theta_c)$. Moreover, eq. 1 is an ellipse expression with the center at (0,0) and axes rotation. Equation 2 is called a *Superellipse* because it has an extra coefficient n_0 which modifies the shape of the formula. The *Supershape* curve (eq. 3) has 5 degrees of freedom and no axes rotation.

After the fitting of all speed lines for the three cases, the equations are then compared regarding their relative Root Mean Squared Error (RMSE). It is observed that the *Ellipse* has the most effective fitting behaviour in low as well as high rotational speeds with a relative RMSE less than 0.9%. Moreover, *Supershape* presented increased error above 1.25%. The satisfactory results of 1 enables us to select it for the modeling of iso-speed lines of the compressor. Then, the coefficients of the adopted formula (α,β,θ) are expressed as a function of reduced shaft speed with the use of a linear interpolation. This interpolation is required in order to link the equations that are fitted in available the speed curves of the performance map data. Therefore, the code is able to calculate the performance parameters at any shaft speed of the operation spectrum. A similar approach is followed for the compressor's isentropic efficiency curves. Three different ellipsoid equations were tested and there the *Superellipse* equation was found to match best with the data for isentropic efficiency. Figure 1 presents the produced compressor map after the fitting and interpolation technique.

A similar method is pursued for the turbine performance map. However, for this specific case, a different group of fitting curves is applied. The distinct shape of the iso-speed lines (Figure 2) in a turbine map allowed us to apply an exponential curve with a rotated axis (eq. 4) and compared it with 4th and 5th degree polynomials (eq. 5 and 6). Equation 4 could only be solved indirectly which makes it computational heavier than the polynomials. Moreover, the exponential curve presented small relative error only in low reduced speed regions. Therefore, the 4th

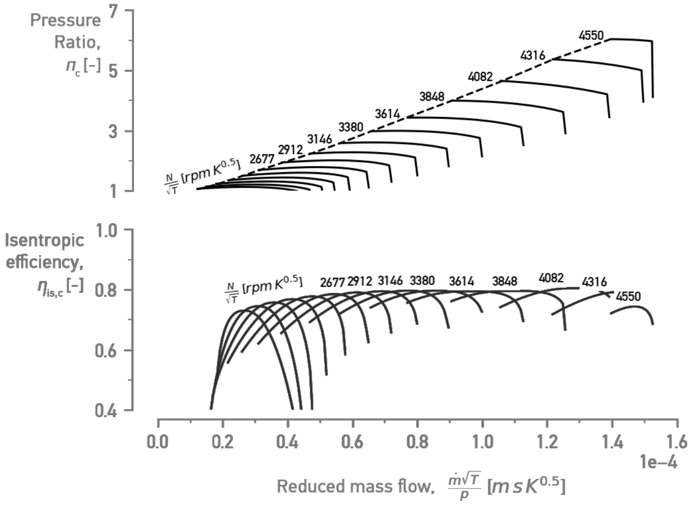

FIGURE 1: Compressor performance map generated by the curve fitting method. The steep decrease in the pressure ratio in each iso-speed line is modeled with a linear interpolation.

degree polynomial equation is adopted to simulate the reduced mass flow rate of the turbine as it showed the most accurate and fast solution compared to the other two cases.

$$Exp: \dot{m}_{t,red}cos(\theta_t) - \pi_t sin(\theta_t) = b_t^{\pi_t cos(\theta_t) - \dot{m}_{t,red} sin(\theta_t)} + c_t \quad (4)$$

$$Poly4: \dot{m}_{t,red} = \alpha_t \pi_t^4 + b_t \pi_t^3 + c_t \pi_t^2 + d_t \pi_t + e_t \quad (5)$$

$$Poly5: \dot{m}_{t,red} = \alpha_t \pi_t^5 + b_t \pi_t^4 + c_t \pi_t^3 + d_t \pi_t^2 + e_t \pi_t + f_t \quad (6)$$

For the efficiency, a two term exponential formula is used as suggested by Tsoutsanis et al. [18]. To illustrate, the turbine map for the entire operation spectrum of the mGT is generated in Figure 2. The model of the turbine map is capable to calculate the reduced mass flow rate and the isentropic efficiency for a specific expansion ratio and $N/\sqrt{T}$.

Modeling approach

This subsection presents the governing equations and calculation techniques used for the prediction of the output parameters of each block as well as the layout of the different modules. At the end, an overview of the system, including all the numbers in each stage of the blocks along with the output, input and boundary conditions are presented in Figure 9.

Turbomachinery blocks The outlet values are determined with the same modeling approach for both the compressor and the turbine. Therefore, the turbomachinery black box model

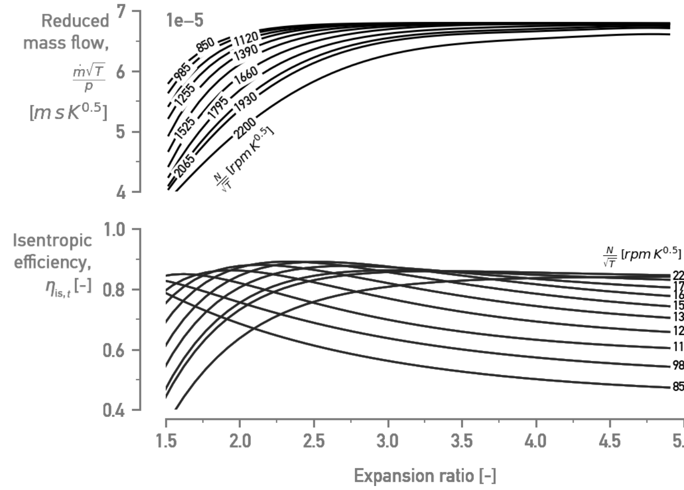

FIGURE 2: The turbine performance map fitting method models smoothly the $\dot{m}_{t,\text{red}}$ and $\eta_{is,t}$.

with the input and output variables is presented in Figure 3 as part of the global mGT model. We assume that the fluid inertia can be neglected inside the control volume. This is supported by the high fluid velocity and by the small component volume compared to the working medium velocity [19, 20]. With this assumption, the mass and energy conservation equations have a steady-state form. Thus the mass flow rate can be calculated using the quasi-steady equations for each time step.

The mass flow rates of these blocks (Compressor, Turbine) are obtained by the utilization of the map equations for a given rotational speed (N) and pressure ratio (π).

$$\dot{m} = f_{\text{map}}\left(\pi, N/\sqrt{T_{in}}\right)\frac{p_{in}}{\sqrt{T_{in}}} \quad (7)$$

Next step is the calculation of outlet temperature (T_{out}). We assumed that the flow is a perfect gas, as the compressibility factor Z is very close to 1 at pressures that reach $6 \cdot 10^5$ Pa. Thus we used the isentropic model to obtain the isentropic temperature ($T_{is,out}$) as

$$T_{is,out} = T_{in}\pi^{(\kappa-1)/\kappa} \quad (8)$$

Then the outlet specific enthalpy is derived from the definition of isentropic efficiency (η_{is}) in eq. 9.

$$h^*_{out} = h_{in} + \frac{h_{is,out} - h_{in}}{\eta_{is}}, \quad (9)$$

where $h_{is,out}$ is obtained from the Coolprop library [21] using the pressure and temperature of the stage as inputs. Finally, we

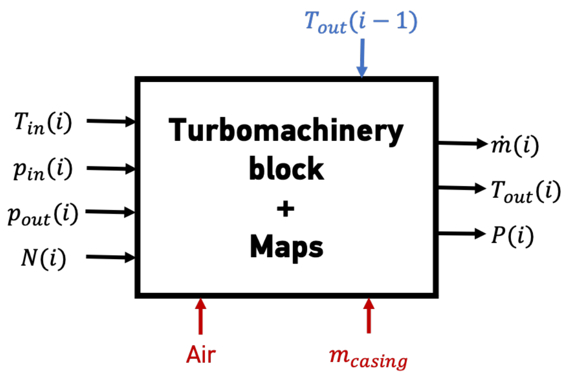

FIGURE 3: Layout of the turbomachinery block (Compressor and Turbine) with the input and output parameters. The constant values are presented in red color and the values of the previous time step with blue color.

calculate the $T*_{out}$ again with the use of Coolprop knowing the specific enthalpy and pressure in the outlet. The specific heat capacity ratio (k) in eq. 8 is defined as

$$\kappa = \frac{\overline{C_p}(T_{in}, T^*_{out})}{\overline{C_v}(T_{in}, T^*_{out})}, \tag{10}$$

where $\overline{C}$ is the average specific heat capacity. As the κ is a function of T_{in} and T^*_{out}, we have used an iterative process between eq. 7, 8 and 9 in order for T_{out} to converge in a specific value.

The thermal capacitance of the block is significant in dynamic conditions. For this reason, we also integrated the heat transfer between the fluid and the component's casing. Thus, we assume that the outlet temperature (T_{out}) is equal to a virtual casing temperature (T_{casing}). As we apply the energy conservation to the virtual casing, we derive the time depended T_{out} as

$$\frac{dT_{out}}{dt} = \frac{\dot{m}(h^*_{out} - h_{out})}{m \cdot c}. \tag{11}$$

In eq. 11, m_{casing} and c_{casing} are the mass and specific heat capacity of the virtual casing. These values are obtained by calibrating this module with experimental results from the T100 test rig.

Recuperator block The Turbec T100 engine works with a heat exchanger which is developed by RSAB and it is particularly designed for mGT applications [22]. The effective modeling of the recuperator requires the discretization of the virtual mass m_r of the component into n cells in order to capture accurately the temperature gradient at the wall $\frac{dT_w}{dt}$ as it is shown in Figure 4.

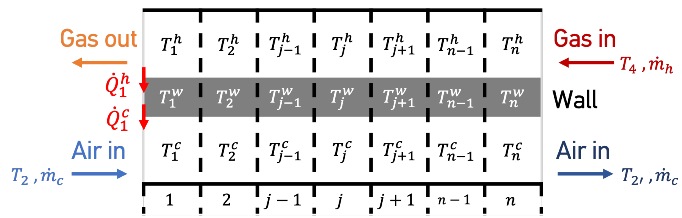

FIGURE 4: Modeling approach of the Recuperator. The virtual heat exchanger model is discritized in n number of cells.

This is justified as 0-D technique assumes a constant wall temperature in the recuperator. Such approach can generate numerical problems and instabilities in dynamics operation especially in compact heat exchangers in which the wall temperature gradient is high [23]. The accuracy of this block is ensured by the use of 5 cells. In each cell, the energy conservation is applied for the wall with the equation below:

$$\frac{m_r c}{n}\frac{dT_w}{dt} = \dot{m}_c C_{p,c}(T^c_{j+1} - T^c_j) - \dot{m}_h C_{p,h}(T^h_{j+1} - T^h_j) \tag{12}$$

The subscripts c and h present the cold and hot stream respectively. Also, c is the heat capacity of the wall. A common practice to calculate the heat fluxes ($\dot{Q}$) and temperatures in each cell is to apply a steady-state approximation for the two streams [6]. Therefore, the heat fluxes in each cell are defined by

$$\dot{Q}^c_{j+1} = \dot{m}_c C_{p,c}(T^c_{j+1} - T^c_j) = \frac{UA}{n}[T^w_j - 1/2(T^c_{j+1} - T^c_j)] \tag{13}$$

$$\dot{Q}^h_{j+1} = \dot{m}_h C_{p,h}(T^h_{j+1} - T^h_j) = \frac{UA}{n}[1/2(T^h_{j+1} - T^h_j) - T^w_j], \tag{14}$$

where the UA represents the heat transfer coefficient times the available surface and is expressed as a function of cold side mass flow rate $\dot{m}_c$. Experimental data were used to make this correlation in four different demanded loads (100, 90, 80, 70 $\mathrm{kW_e}$). Thus, the UA is changed and tuned to match until the effectiveness ($\varepsilon = (T^c_{out} - T^c_{in})/(T^h_{in} - T^c_{in})$) of the simulation matches the results from experiments. Then the intermediates are calculated with a linear interpolation of the tuned UA points.

In the current study, the calculation time of the dynamic mGT software is of significant importance. We want to make sure that the indicated solution approaches are not computationally heavy. The solution strategy of the Ordinary Differential Equations (ODE) plays an important role in the determination of the calculation time. For this reason, we tested two different ODE solution schemes for eq. 12 and compared them regarding their computational time on the same computer. A classic Forward Euler solution and a Python built-in function called

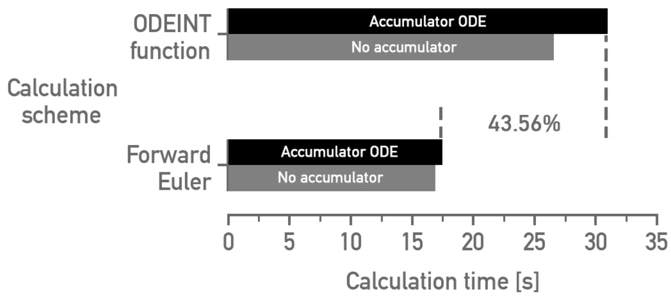

FIGURE 5: Comparison of the calculation time between two different ODE solving techniques. A simpler solving approach (Forward Euler) decreases the calculation time without jeopardising the accuracy.

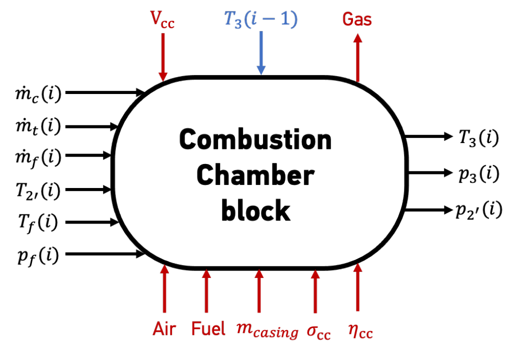

FIGURE 6: Layout of the Combustion Chamber block with the input and output parameters. This module basically calculates the pressure and temperature in the outlet of the CC.

ODEINT were applied. The Forward Euler uses a step by step solution contrary to the *ODEINT* which implements a multi-step approach. The two schemes are also compared when we also add an accumulator in the recuperator block with eq. 11. The results of these two approaches are presented in Figure 5.

Figure 5 shows that the calculation time, with (black bars) or without (grey bars) an ODE for the accumulator, is quite low in the Forward Euler solution. More specifically, the difference in calculation time between the two methods, when we solve eq. 11 and 12, reaches 43.56%. Thus the Forward Euler approach is applied for the solution of ODEs in the code as not only it decreases the calculation time but it also removes the added complexity of a multi-step solution. Moreover, no accumulator is finally used in the recuperator block, since by just solving eq. 12, the code predicted satisfactorily the evolution of temperatures in time. This is thoroughly explained in the Results and Discussion section.

Combustion Chamber block The boundary conditions of the Combustion Chamber (CC) block are shown in Figure 6 using red arrows along with the input and output parameters on the left and right hand side, respectively.

This module calculates the mass conservation inside the CC, which is described below as

$$\frac{d\rho_3}{dt} = (\dot{m}_f + \dot{m}_c - \dot{m}_t)/V_{cc} \tag{15}$$

where ρ_3 is the density in the CC outlet and V_{cc} the volume of the component. This block also solves the energy conservation equation, which is as presented as

$$\frac{du_3}{dt} = \frac{\dot{m}_f(h_f + LHV\eta_{cc}) + \dot{m}_c h_{2'} - \dot{m}_t h_3 - u_3 \Delta\dot{m}_{cc}}{V_{cc}\rho_3}. \tag{16}$$

The difference between the inlet and outlet in mass flow rate is $\Delta\dot{m}_{cc} = \dot{m}_f + \dot{m}_c - \dot{m}_t$, LHV equals the Lower Heat Value of the fuel, and η_{cc} represents the combustion efficiency. Also, h is the specific enthalpy of the 3 different flows and u_3 equals the specific internal energy of the flue gasses (subscript f) at the combustor outlet. The pressure (p_3) and temperature (T_3) at the outlet are calculated form the Coolprop thermodynamic library after we determine the u_3 and ρ_3. The CC block also accounts for the thermal resistance of the chamber by solving eq. 11 and using the temperature of the previous time step presented with a blue arrow in Figure 6.

Shaft block The rotational speed of the shaft is also governed by a differential equation and includes the terms of the power that is generated and consumed during a dynamic operation. The equation that describes this energy conservation is described as

$$\frac{d\omega}{dt} = \frac{P_t - P_c - P_{lb} - P_{le} - P_{load}}{I\omega}, \tag{17}$$

where ω is the shaft angular speed, I is the moment inertia of the shaft, P_t is the power produced by the turbine, P_c the power absorbed by the compressor, P_{lb} the power losses from the bearings, P_{le} the consumption of the power electronics and auxiliaries and finally P_{load} is the power produced by the generator, which is regulated by the control system. For the bearing losses, a model presented by Henke et al. is adopted [15]. For the electrical losses and auxiliaries, a correlation is made using experimental data from the Turbec T100 test rig. This correlation is a function of P_{load} and a 3rd degree polynomial. We also modeled the generator with an electrical efficiency of 99% and the power electronics with a conversion efficiency of 95%. All the inputs, outputs and boundary conditions are presented in Figure 9.

Control system block In our work the term "real-time" is related with the fact that the model simulates the same timeframe as the experiments. The code does not run as fast as the real application so that we can use it to get control data for as a digital twin. It runs to calculate performance results within a few minutes. Thus, we do not use it directly for control purposes. The Turbec T100 control system is divided in two main parts, the fuel control and the power control. The fuel control consists of a Turbine Outlet Temperature (TOT) control loop which keeps the TOT constant during the simulation. At first, the fuel requirement is determined from the TOT and the ambient temperature (T_{amb}). Next, based on the shaft speed, a primary value of the fuel requirement is calculated from a table given by the manufacturer. Then the TOT fuel requirement is added in the primary value, and added to an integrator of the TOT fuel requirement to get finally the total fuel necessary. The scheme of this fuel control is presented in Figure 7.

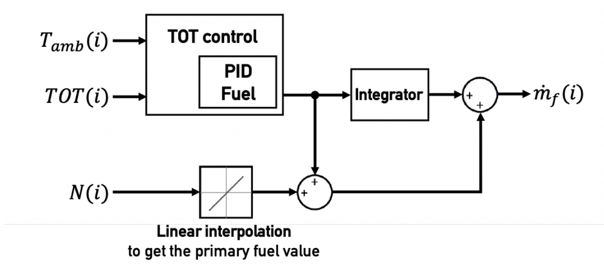

FIGURE 7: Layout of the fuel control. The main regulators of the fuel flow rate are the shaft speed and the TOT error signal.

The power control has the demanded power (P_{dem}) as input. The controller links P_{dem} with a reference shaft speed by look-up tables. Then this speed is regulated by a controlled fault signal between P_{dem} and P_{load} of the previous time step. Afterwards, the corrected reference speed is compared with the simulated shaft speed (N). The error signal generated, controls the P_{load} which is then converted from kW to W by adding a gain with the value of 1000. This strategy is presented as a layout in Figure 8.

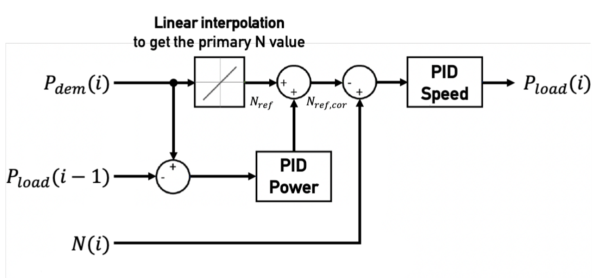

FIGURE 8: Layout of the power control, The reference speed is calculated and then it is adjusted based on the error signal.

Model structure

The integration of each module that was describe above into a complete real-time software requires to solve 11 different ODEs relatively fast. The complete model is shown in Figure 9 as a block diagram to have a full picture of the inputs, outputs, boundary conditions. The relation between different components is also depicted with arrows that link the inputs and outputs.

RESULTS AND DISCUSSION

In order to prove the accuracy of the developed model, at first, a steady state validation is performed in 4 different generated powers (100, 90, 80, 70 kW_e) by comparing the crucial values of the engine with the data from the VUB test rig of Turbec T100 [8, 24]. Finally, the generated values are tested concerning their fidelity to transient experimental data taken from the T100.

The test rig, located in VUB laboratory, is a series 2 Turbec T100 mGT. It has a nominal electric power and a thermal power output of 100 kW_e and 165 kW_{th} respectively. The maximum rotational speed is close to 70 000 rpm at nominal conditions. Also, the TOT is controlled and fixed at around 645 °C by regulating the fuel flow rate to preserve a high electrical efficiency. The air flow goes inside the compressor in stage **1** (Figure 9) and leaves at stage **2** with increased pressure. Then, additional heat is added into the working fluid inside the recuperator between stages **2** and **2'**. The energy of the fluid significantly increases inside the Combustion Chamber (stages **2'** to **3**). The turbine expands the flow and produces useful work from **3** to **4**. Finally, the expanded gas releases more heat to the air flow before the CC inside the recuperator hot side (stage **4** to **4'**). This machine is operated in both dry and humid modes regarding the working fluid. The list of sensors installed and utilized for the current study in dry mGT operation are shown in Table 1. Also, the frequency of the the measurements is 10Hz.

TABLE 1: Information and accuracy of the censors/measured parameters

Name	Location	Accuracy
T_1	Compressor inlet	$\pm 2^oC$
T_2	Compressor outlet	$\pm 1\%$
T_2'	Combustion Chamber inlet	$\pm 0.4\%$
T_4	Turbine outlet	$\pm 0.4\%$
T_4'	Recuperator hot side outlet	$\pm 0.55^oC$
p_2	Compressor outlet	$\pm 150 Pa$
N	Controller	$\pm 0.1\%$
P_{load}	Controller	$\pm 1\%$
$\dot{m}_f$	Combustion Chamber fuel inlet	$\pm 1\%$

Steady state results

We performed a steady state validation to the in-house mGT model against the data that has been gathered at VUB test rig.

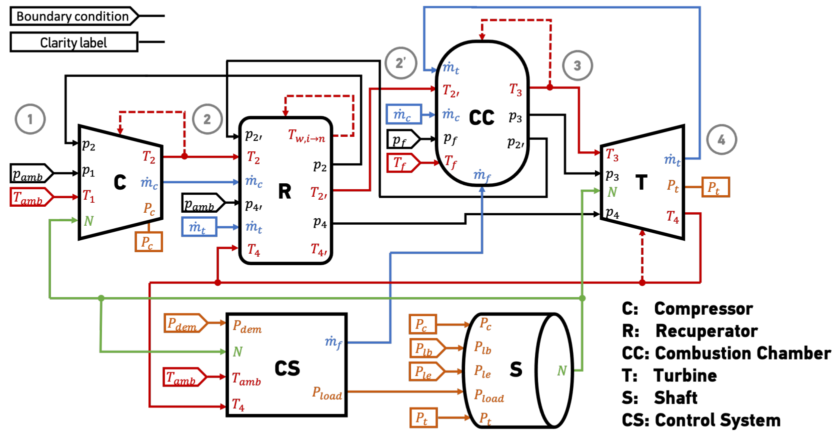

FIGURE 9: Layout of the mGT model presented as block diagram. Pressure streams are shown in black, Temperature in red, Mass flow in blue, Power in orange and Shaft speed in green. The dashed lines present the feedback loops of the previous time step i-1.

Therefore, we carried out four steady-state tests with a generated load (P_{load}) of 100, 90, 80 and 70 kW$_e$. The tests were executed at an average ambient temperature (T_{amb}) of 21.2 °C. The values that are used for this validation are $N, \dot{m}_f, T_2, p_2, T_{2'}$. The accuracy of these measurements is shown in Table 1. The electric efficiency is calculated as

$$\eta_{el} = \frac{P_{load} - P_{aux}}{\dot{m}_f LHV} \tag{18}$$

and also used in the validation. The testing of these parameters seem sufficient to make a solid conclusion for the accuracy of the simulation in steady-state conditions. Figure 10 presents the steady state results for the rotational speed and electrical efficiency of the model along with the the experimental data. This way, we can examine how the simulation matches the the measured data. First of all, the rotational speed follows the same trend as the measurements quite well. The values at 100, 90 and 70 kW$_e$ fit satisfactorily the experiment. There is a small deviation at 80 kW which can be associated with the use of the performance maps given by the manufacturer. The actual turbomachinery maps in the test rig are possibly slightly modified due to engine degradation. The electrical efficiency results also follow closely the experiments. The small difference that is observed is linked to the calculation of power losses in model rather than to

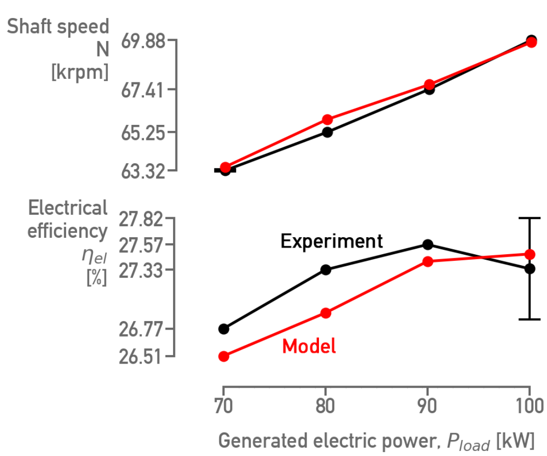

FIGURE 10: Steady state results of rotational speed (N) and electrical efficiency (η_{el}) at four power loads (P_{load}). The largest deviation of the Model (black color) from experiments (red color) is observed at 80 kW$_e$

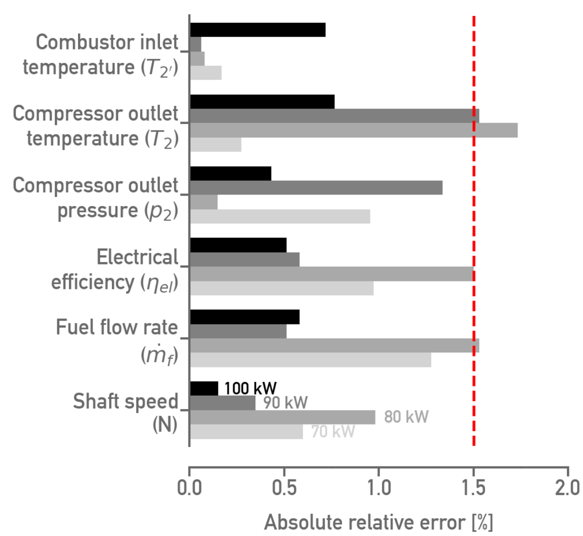

FIGURE 11: Percentage error of the values used for the steady state validation. Almost all the values have an error below the range of accuracy of the measuring probes.

the fuel flow rate. The results of fuel flow rate present a deviation below 1.5%, which seems reliable. Moreover, the simulated efficiency remains in the range of the measurement uncertainties. As a result the model shows a decent performance prediction.

Figure 11 presents the relative error of the values that are tested during the validation process altogether in the four different generated power loads. The relative error is measured in eq. 19.

$$e = \frac{|x_m - x|}{x_m} 100\% \tag{19}$$

The simulated values are shown as x and the measured ones as x_m.

Most of the values in Figure 11 show errors below 1.5%. $T_{2'}$ presents errors below 1% which confirms the accurate modelling of the recuperator component. Furthermore, it is shown that fuel flow rate, efficiency and shaft speed has the largest error at 80 kW$_e$. Although, this error does not exceed the 1.5% limit. This limit is considered to be in the range of accuracy of the measurement probes and is consider to be reliable for GT operations.

The compressor outlet temperature shows deviation from the measurements above 1.5% at 80 kW$_e$. This error does not exceed 2% (1.73%) and can be linked, through the isentropic law, to the change of the map values due to performance deterioration. This is explained previously for the shaft speed results. Also, this error does not propagate to the recuperator component. As a result, the model is observed to fit the experimental results quite accurately. In order to confirm the accuracy and get a more extensive understanding of the models fidelity, it is crucial to test the transient behaviour of the model's important parameters.

Transient results

During the experimental tests we took the demanded power (P_{dem}) as an input in the control system block of the model. Several parameters are observed during two step changes in the demanded power. The first step is considered to be 100-80 kW$_e$ (-20 kW$_e$) and the second 90-100 kW$_e$ (+10 kW$_e$). We performed a correlation of T_1 as a function of time to account for the increase in compressor inlet temperature during the operation of the engine. Also, the ambient pressure (p_{amb}) is set to 101 020 Pa. The evolution of of each parameter during the two steps will be presented and discussed in detail to confirm the accuracy of each component simulation.

The control system calculates the generated power of the engine inside the power control block (Figure 8). Figure 12 shows the simulated values in red and the experimental results in black at +10 kW$_e$ and [b] -20 kW$_e$ step of the generated electrical power. It is observed that in both steps, the calculated steady-state values correspond with the measurements. Moreover, we can see that the simulated slopes follow the behaviour of experiments nicely. In Figure 12 [a] the model follows the measurements until the the peak. After that, the data present a more decreasing behaviour compared to the model, where the curve of the model at 100 kW$_e$ is more flat. This behaviour is justified as additional power is produced because more fuel is added. This will be thoroughly explained in the next figure. At -20 kW$_e$ step, the simulation achieves to capture well the downward and upward peaks during the transition of power. However, a small displacement is observed in the slope before the downward peak. Also the downward peak in Figure 12 [b] is slightly larger. The difference in peaks could be explained by the noise of the measured value. This figure confirms that the power control block of the simulation models almost precisely predicts the behaviour of the actual controller of the engine.

The other crucial parameter that can verify the effective behaviour of the virtual control system is the fuel flow rate. This value is responsible for correctly regulating the energy and mass conversation inside the combustion chamber and eventually adjusting the TOT and p_3. Figure 13 shows the evolution of fuel

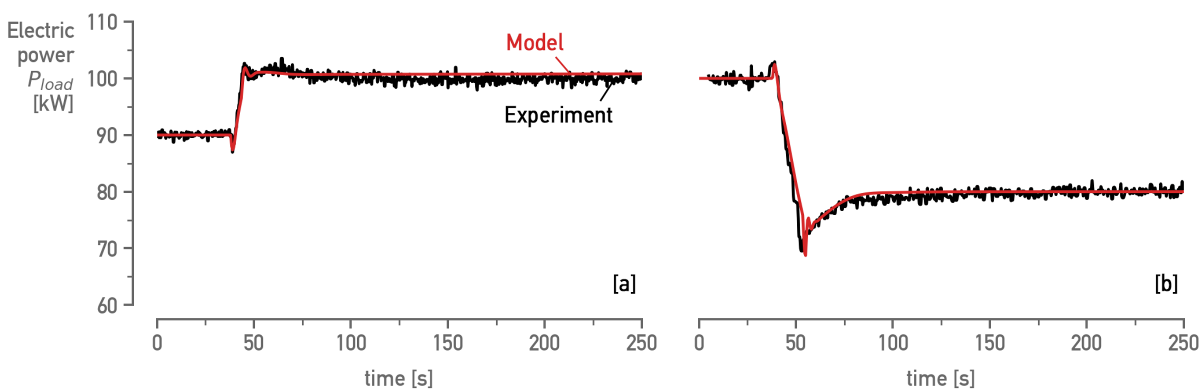

FIGURE 12: Produced electric power (P_{load}) in a [a] +10 kW$_e$ and [b] -20 kW$_e$ step change. The model at [a] shows a less decreasing behaviour in power from 60 to 250s.

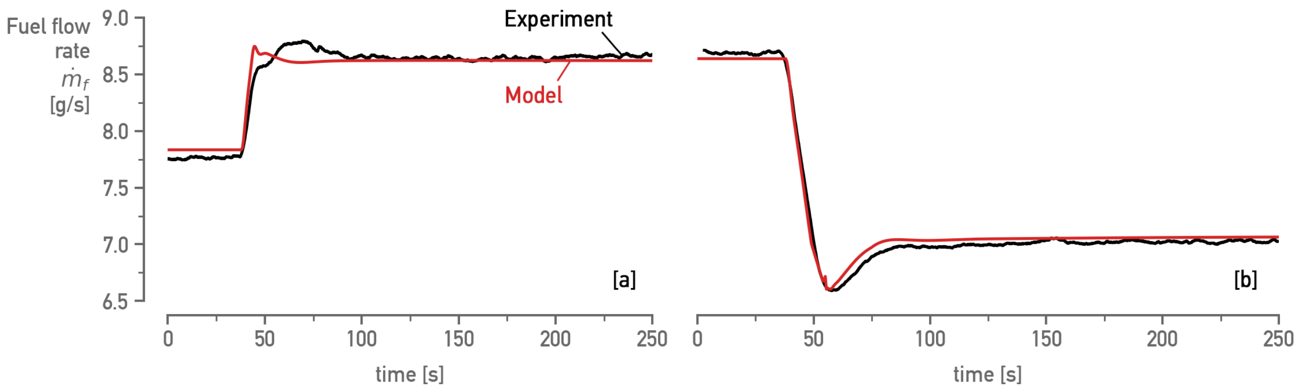

FIGURE 13: Fuel flow rate ($\dot{m}_f$) in a [a] +10 kW_e and [b] −20 kW_e step change. The model at [a] (90 kW) shows a larger peak and steeper decrease from 40 to 60 s compared to experiments.

flow rate through time at the two steps in demanded power. Fuel flow rate shows a small deviation from experiments before and after the steps at 0 and 250 s respectively. This difference is presented in the previous section. In both steps the slope during the transient follows adequately the measurements. In Figure 13 [a] there is a relatively higher fuel flow rate immediately after the transition (45-50 s). The peak continues to increase during the simulation, while in the measurements the peak occurs after 10 s. The modelled mass flow behaves in a such way that is causes a less decreasing produced power. This was observed in Figure 12 [a]. This mismatch in mass flows, after the transition, very quickly dissipates before the 100 s mark. Then, the mass flow accurately follows the data. In Figure 13 [a] the model simulates flawlessly the transition. At 80 kW_e there is a small deviation in the calculated fuel flow which does not exceed the 1.6% limit. Thus, we can see that the fuel control module accurately predict the mass flow rate for a negative step change but miscalculates the peaks at the positive step. This does not prevent the control system to provide the correct amount of fuel in the cycle before and after the peak.

The rotational speed of the engine is measured at the shaft and Figure 14 shows the experimental data along with the simulated results in the two considered power steps. Again the slope of the transition is followed well by the simulated rotational speed in both steps. Figure 14 [b] shows a decreased peak in N compared to the measured data. This behaviour is also observed in the P_{load} results and it is caused by the control system. Another possible root for this phenomenon is the deviation of the used compressor map from the actual turbomachinery performance characteristics. The largest deviation of the rotational speed is presented in Figure 14 [b] in which the model overestimates N at 80 kW_e. Moreover, the downward peak is quite smaller (63.95 rpm). The rotational speed is connected with the performance maps in the model. So, any change in the outlet pressure of the turbomachinery components affects the shaft speed. The current test rig was converted to a mHAT. When we operate it in dry conditions extra pressure and heat losses are added to the system compared to a typical T100 mGT due to the additional tubing.

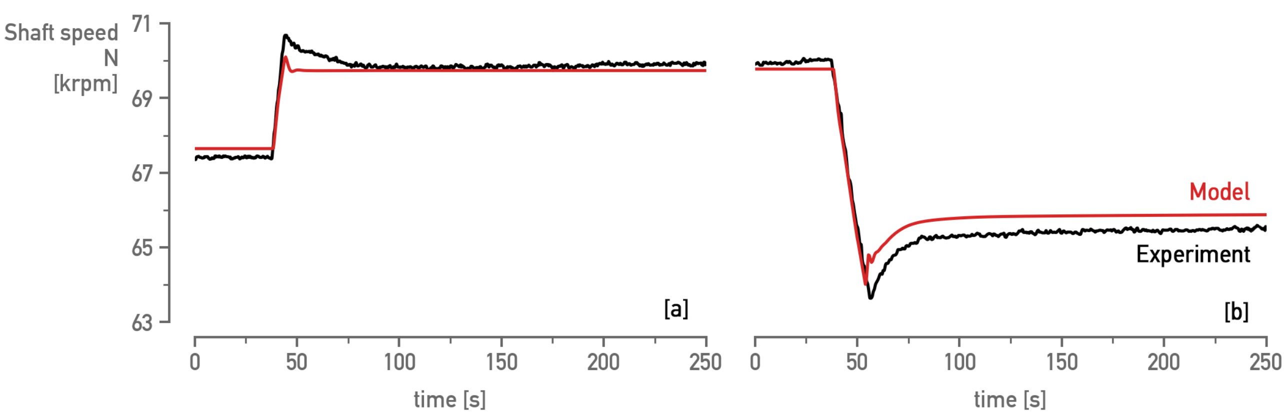

FIGURE 14: Rotational speed (N) in a [a] +10 kW_e and [b] −20 kW_e step change. The model overestimates N at 80 kW_e.

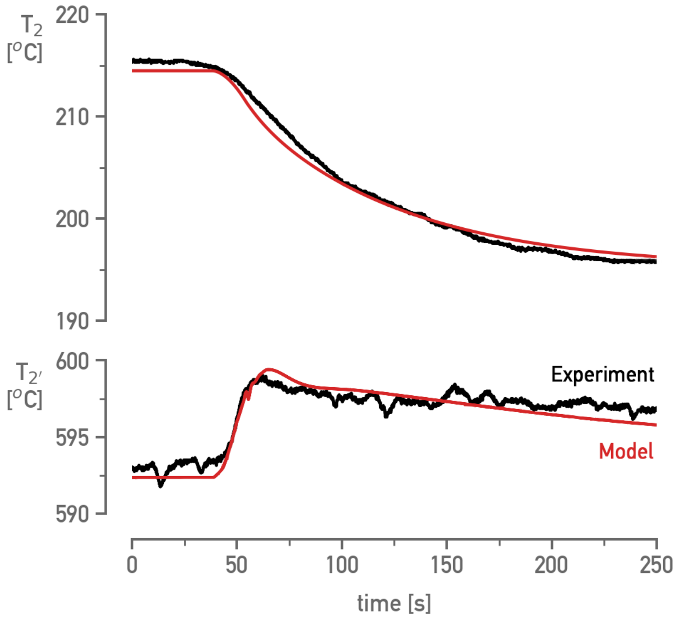

FIGURE 15: Compressor outlet temperature T_2 and Recuperator outlet temperature $T_{2'}$ at a $-20\,\mathrm{kW_e}$ step (100-80 $\mathrm{kW_e}$). The calibration of mass of the casings and the UA produced satisfying results.

Therefore, this behaviour is attributed to a slight miscalculation of the pressure losses in part load. Moreover, as we described above, the performance maps that are used, play a crucial role in correct calculation of N. Therefore, the results present an accurate enough behaviour to model mGT cycles. In Figure 15 we observe the evolution of compressor outlet T_2 and recuperator outlet $T_{2'}$ temperatures at a $-20\,\mathrm{kW_e}$ load step change. It is clear that the temperatures have a smoother dynamic response compared to all the other performance values presented above. This is a result of the large thermal inertia of the components' casing. As it was mentioned in previous chapter, both casing masses were calibrated to accurately match the characteristic dynamic responses. The error of T_2 does not exceed 3°C. The virtual mass of the compressor's casing is chosen at 105 kg which allowed the results to predict adequately the trend of the experiments.

The recuperator cold side outlet temperature $T_{2'}$ is also presented in Figure 15. This temperature is measured with 2 thermocouples in two opposite places in the recuperator outlet and an average value is presented [24]. This temperature is closely dependant on the T_2, the TOT and the heat transfer coefficient (UA). The TOT is controlled by the fuel flow and affects the transition slope of $T_{2'}$. Moreover, the UA plays an important role on the amount of heat that is added in the flow. From Figure 15 it is obvious that our strategy to use a variable UA that is a function of air flow, allowed us to model the $T_{2'}$ accurately. The simulated $T_{2'}$ follows well the experiment not only in constant power but also during the transition. Although, the peak of $T_{2'}$ is slightly higher, this result is in the range of the measured uncertainties.

CONCLUSIONS

In the current work, we aimed to effectively model the dynamic behaviour of mGT cycles. A detailed, and modular mGT dynamic model developed in Python programming language is explained thoroughly. We presented the calculation methods that were used for each component of the cycle. Our main objective was to decrease the complexity and the computation time of the calculations. Specific attention was given to the correct and smooth modelling of the performance maps. Fitting equation were compared and the most accurate one was adopted in the model. We used an 1-D model for the recuperator with variable UA and we examined two distinctive differential equations solvers regarding their calculation speed. Therefore, a simple Forward Euler step by step solver is chosen for the 10 different ODEs of the model.

We validated the model in steady-state conditions for 4 different generated powers. The model was compared with experimental results gathered from the Turbec T100 test rig in VUB. The simulated results showed a good agreement with the measured data. Most of the obtained errors of the compared values are below the 1.5% limit. Also, the calculated values remained within the range of the uncertainties of the measurements. Additionally, we compared the crucial parameters of the model with the measurements in transient operation at two different step changes in demanded power. The transient result presented a good agreement with the data with only minor deviations. The deviations in fuel flow rate are attributed to the behaviour of the fuel control system. Moreover, the small miscalculation of the rotational speed has to do with the modelling of the pressure losses in part load. As a future step, these losses could be recalculated and a correlation can be drafter based on experimental data. With this method we can match the additional pressure losses which were introduced with the conversion of this mGT to a mHAT.

ACKNOWLEDGMENT

NextMGT has received funding from the European Union's Horizon 2020 research and innovation programme under Marie Sklodowska - Curie grant agreement No 861079.

REFERENCES

[1] Xiao, G., Yang, T., Liu, H., Ni, D., Ferrari, M. L., Li, M., Luo, Z., Cen, K., and Ni, M., 2017. "Recuperators for micro gas turbines: A review". *Applied Energy,* **197**(C), pp. 83–99.

[2] Caresana, F., Pelagalli, L., Comodi, G., and Renzi, M., 2014. "Microturbogas cogeneration systems for distributed generation: Effects of ambient temperature on global performance and components' behavior". *Applied Energy,* **124**(C), pp. 17–27.

[3] Ismail, M., Moghavvemi, M., and Mahlia, T., 2013. "Current utilization of microturbines as a part of a hybrid system in distributed generation technology". *Renewable and Sustainable Energy Reviews,* **21**(C), pp. 142–152.

[4] Kolanowski, B. F., 2004. *Guide to microturbines*. Lilburn, GA: New York: Fairmont Press.

[5] Comodi, G., Renzi, M., Caresana, F., and Pelagalli, L., 2015. "Enhancing micro gas turbine performance in hot climates through inlet air cooling vapour compression technique". *Applied Energy,* **147**(C), pp. 40–48.

[6] Duan, J., Sun, L., Wang, G., and Wu, F., 2015. "Nonlinear modeling of regenerative cycle micro gas turbine". *Energy,* **91**, pp. 168–175.

[7] Pepermans, G., Driesen, J., Haeseldonckx, D., Belmans, R., and D'haeseleer, W., 2005. "Distributed generation: definition, benefits and issues". *Energy Policy,* **33**(6), pp. 787–798.

[8] De Paepe, W., Carrero, M. M., Bram, S., Parente, A., and Contino, F., 2014. "Experimental characterization of a t100 micro gas turbine converted to full humid air operation". *Energy Procedia,* **61**, pp. 2083–2088. International Conference on Applied Energy, ICAE2014.

[9] MosayebNezhad, M., Mehr, A., Lanzini, A., Misul, D., and Santarelli, M., 2019. "Technology review and thermodynamic performance study of a biogas-fed micro humid air turbine". *Renewable Energy,* **140**, sep, pp. 407–418.

[10] Ferrari, M. L., Silvestri, P., Pascenti, M., Reggio, F., and Massardo, A. F., 2017. "Experimental Dynamic Analysis on a T100 Microturbine Connected With Different Volume Sizes". *Journal of Engineering for Gas Turbines and Power,* **140**(2), 10.

[11] Calabria, R., Chiariello, F., Massoli, P., and Reale, F., 2015. "CFD Analysis of Turbec T100 Combustor at Part Load by Varying Fuels". Vol. Volume 8: Microturbines, Turbochargers and Small Turbomachines; Steam Turbines of *Turbo Expo: Power for Land, Sea, and Air*.

[12] di Gaeta, A., Reale, F., Chiariello, F., and Massoli, P., 2017. "A dynamic model of a 100 kW micro gas turbine fuelled with natural gas and hydrogen blends and its application in a hybrid energy grid". *Energy,* **129**(C), pp. 299–320.

[13] Traverso, A., 2005. "TRANSEO Code for the Dynamic Performance Simulation of Micro Gas Turbine Cycles".

[14] Ghigliazza, F., Traverso, A., Pascenti, M., and Massardo, A. F., 2009. "Micro Gas Turbine Real-Time Modeling: Test Rig Verification". Vol. Volume 5: Microturbines and Small Turbomachinery; Oil and Gas Applications of *Turbo Expo: Power for Land, Sea, and Air*, pp. 29–36.

[15] Henke, M., Monz, T., and Aigner, M., 2016. "Introduction of a New Numerical Simulation Tool to Analyze Micro Gas Turbine Cycle Dynamics". *Journal of Engineering for Gas Turbines and Power,* **139**(4), 11.

[16] Blotenberg, W., 1993. "A Model for the Dynamic Simulation of a Two-Shaft Industrial Gas Turbine With Dry Low NOx Combustor". Vol. Volume 3C: General of *Turbo Expo: Power for Land, Sea, and Air*.

[17] Bettocchi, R., Spina, P. R., and Fabbri, F., 1996. "Dynamic Modeling of Single-Shaft Industrial Gas Turbine". Vol. Volume 4: Heat Transfer; Electric Power; Industrial and Cogeneration of *Turbo Expo: Power for Land, Sea, and Air*.

[18] Tsoutsanis, E., Meskin, N., Benammar, M., and Khorasani, K., 2015. "Transient Gas Turbine Performance Diagnostics Through Nonlinear Adaptation of Compressor and Turbine Maps". *Journal of Engineering for Gas Turbines and Power,* **137**(9), 09.

[19] Camporeale, S. M., Fortunato, B., and Dumas, A., 2000. "Dynamic modelling of recuperative gas turbines". *Proceedings of the Institution of Mechanical Engineers, Part A: Journal of Power and Energy,* **214**(3), pp. 213–225.

[20] Kim, M. J., Kim, J. H., and Kim, T. S., 2016. "Program development and simulation of dynamic operation of micro gas turbines". *Applied Thermal Engineering,* **108**, pp. 122–130.

[21] Bell, I. H., Wronski, J., Quoilin, S., and Lemort, V., 2014. "Pure and pseudo-pure fluid thermophysical property evaluation and the open-source thermophysical property library coolprop". *Industrial & Engineering Chemistry Research,* **53**(6), pp. 2498–2508.

[22] Lagerström, G., and Xie, M., 2002. "High Performance and Cost Effective Recuperator for Micro-Gas Turbines". Vol. Volume 1: Turbo Expo 2002 of *Turbo Expo: Power for Land, Sea, and Air*, pp. 1003–1007.

[23] McDonald, C. F., 2003. "Recuperator considerations for future higher efficiency microturbines". *Applied Thermal Engineering,* **23**(12), pp. 1463–1487.

[24] Montero Carrero, M., De Paepe, W., Magnusson, J., Parente, A., Bram, S., and Contino, F., 2017. "Experimental characterisation of a micro humid air turbine: assessment of the thermodynamic performance". *Applied Thermal Engineering,* **118**, pp. 796–806.